

ORDER, DISORDER, AND PHASE TRANSITION IN CONDENSED SYSTEM

Crystal Structure and Magnetization of a $\text{Co}_3\text{B}_2\text{O}_6$ Single Crystal

N. V. Kazak^a, M. S. Platonov^{a,*}, N. B. Ivanova^b, Yu. V. Knyazev^a, L. N. Bezmaternykh^a, E. V. Eremin^a,
A. D. Vasil'ev^{a,b}, O. A. Bayukov^a, S. G. Ovchinnikov^{a,b,c}, D. A. Velikanov^a, and Ya. V. Zubavichus^d

^aKirensky Institute of Physics, Siberian Branch, Russian Academy of Sciences, Akademgorodok, Krasnoyarsk, 660036 Russia

*e-mail: platonov@iph.krasn.ru

^bSiberian Federal University, Svobodny pr. 79, Krasnoyarsk, 660074 Russia

^cKrasnoyarsk State Aerospace University, Krasnoyarsk, 660014 Russia

^dRussian Research Centre Kurchatov Institute, pl. Akademika Kurchatova 1, Moscow, 123182 Russia

Received July 27, 2012

Abstract—The crystal structure and magnetic properties of $\text{Co}_3\text{B}_2\text{O}_6$ single crystals are studied. Orthorhombic symmetry with space group $Pn\bar{m}$ is detected at room temperature. The measurements of static magnetization and dynamic magnetic susceptibility reveal two magnetic anomalies at $T_1 = 33$ K and $T_2 = 10$ K and an easy-axis magnetic anisotropy. The effective magnetic moment indicates a high-spin state of the Co^{2+} ion. A spin-flop transition is found at low temperatures and $H_{\text{sf}} = 23$ kOe. EXAFS spectra of the K -edge absorption of Co are recorded at various temperatures, the temperature-induced changes in the parameters of the local environment of cobalt are analyzed, and the effective Co–Co and Co–O distances are determined. The magnetic interactions in the crystal are analyzed in terms of an indirect coupling model.

DOI: 10.1134/S1063776113060186

1. INTRODUCTION

Transition metal oxyborates have long been attracted great interest due to a unique combination of their magnetic, optical, magnetoelastic, magneto-optical, and resonance properties. Recent interest in these materials is also related to searching for new multiferroics. For example, ferroelectric ordering, which coincides with a spin-reorientation transition, has recently been detected in a number of $\text{ReFe}_3(\text{BO}_3)_4$ (Re is a rare-earth metal) borates [1, 2]. Another field of investigations is associated with the effects of relation between the charge, spin, and orbital degrees of freedom under a high pressure. Recent studies [3, 4] of magnetic M^{3+}BO_3 ($\text{M}^{3+} = \text{Fe}, \text{V}$) oxyborates revealed a sharp shift in the optical absorption edge, which is accompanied by the collapse of the magnetic moment of the Fe^{3+} ion.

Synthetic borate crystals have a number of promising physical properties and are considered as potential objects for a practical application as magnetically controlled acoustic filters, ionizing radiation detectors, generators, frequency transducers, and so on [5, 6].

Despite the variety of these properties, these compounds are characterized by the following common properties: low crystal lattice symmetry (mainly monoclinic or orthorhombic) and a complex unit cell composition, which has both purely covalent chemical bonds inside boron–oxygen anion groups and relatively weak ionic bonds between a cation and the corresponding anion group. The last circumstance favors carrier localization and a dielectric ground state.

The existence of nonequivalent crystallographic positions and different probabilities of their occupation with metallic ions of the same (M) or different kinds (M, M') make it possible to observe magnetic behavior of various types, namely, from a long-range magnetic order in homometallic oxyborates ($\text{M} = \text{M}'$) [7–9] to the state of spin glass in heterometallic compounds ($\text{M} \neq \text{M}'$) [10, 11].

Orthoborates $\text{M}_{3-x}\text{M}'_x\text{B}_2\text{O}_6$ ($\text{M}, \text{M}' = \text{Co}, \text{Mn}, \text{Ni}, \text{Mg}, \text{Cu}, \text{Cd}$) have orthorhombic (space group $Pn\bar{m}$), triclinic ($P\bar{1}(2)$), and monoclinic ($P2_1/c$) crystal systems (Table 1). Orthorhombic borates $\text{M}_3\text{B}_2\text{O}_6$ are isostructural to mineral kotoite. The following four homometallic ($\text{M} = \text{M}'$) kotoites are known: $\text{Co}_3\text{B}_2\text{O}_6$, $\text{Ni}_3\text{B}_2\text{O}_6$, $\text{Mn}_3\text{B}_2\text{O}_6$, and $\text{Mg}_3\text{B}_2\text{O}_6$ [12–16]. The information on the properties of these materials is very scarce and it mainly concerns crystal chemistry aspects. The authors of [14] studied the crystal structure of kotoite single crystals with $\text{M} = \text{M}' = \text{Mg}, \text{Co}, \text{and Ni}$. They determined atomic coordinates, interatomic distances, and the parameters of isotropic and anisotropic displacements of Mg, Co, Ni, B, and O atoms. The authors of [17, 18] synthesized substituted cobalt-based $\text{Co}_{3-x}\text{Ni}_x\text{B}_2\text{O}_6$ kotoites, studied their structure, and found that an orthorhombic structure isostructural to $\text{Co}_3\text{B}_2\text{O}_6$ forms up to a substitution level $x = 2.0$. As follows from Table 1, the change in the lattice parameter in the series of orthorhombic kotoites correlates with the increase in the ionic radius of a divalent ion. In the case of $\text{M}^{2+} = \text{Cu}$,

Table 1. Crystal lattice parameters of $\text{M}_3\text{B}_2\text{O}_6$ oxyborates

		a , Å	b , Å	c , Å	α, β, γ	V , Å ³
$\text{Ni}_3\text{B}_2\text{O}_6$	Single crystals [12, 14]	$Pn\bar{m}n$ 4.459	5.396	8.297	—	199.63
	Polycrystals [13]	4.490	5.395	8.391		
$\text{Mg}_3\text{B}_2\text{O}_6$	Single crystals [14, 15]	$Pn\bar{m}n$ 4.497	5.398	8.416	—	204.29
	Polycrystals [13]	$Pn\bar{m}n$ 4.529	5.462	8.436		
$\text{Mn}_3\text{B}_2\text{O}_6$	Polycrystals [13]	$Pn\bar{m}n$ 4.648	5.675	8.695	—	229.35
	[16]	4.646	5.658	8.740		
$\text{Co}_2\text{NiB}_2\text{O}_6$	Polycrystals [17]	$Pn\bar{m}n$ 4.504	5.444	8.404	—	206.06
$\text{CoNi}_2\text{B}_2\text{O}_6$	Polycrystals [18]	$Pn\bar{m}n$ 4.478	5.419	8.352	—	202.67
$\text{Cu}_3\text{B}_2\text{O}_6$	Single crystals [19, 20]	$P\bar{1}(2)$ 3.344	19.757	19.587	$\alpha = 88.91^\circ$ $\beta = 70.05^\circ$ $\gamma = 69.93^\circ$	1135.46
$\text{Cu}_2\text{CoB}_2\text{O}_6$	Polycrystals [21]	$P2_1/c$ 3.225	14.849	9.114	$\beta = 93.69^\circ$	435.55
	Single crystals [22]					
$\text{Cu}_2\text{NiB}_2\text{O}_6$	Polycrystals [23]	$P2_1/c$ 3.205	14.838	9.064	$\beta = 93.77^\circ$	430.11
$\text{Cu}_2\text{CdB}_2\text{O}_6$	Polycrystals [24]	$P2_1/c$ 3.419	15.137	9.31	$\beta = 93.05^\circ$	481.14

Note: For convenience and uniformity, we redenoted lattice parameters a^* , b^* , and c^* found for the orthorhombic phase in the literature ($a \rightarrow b^*$, $b \rightarrow c^*$, $c \rightarrow a^*$).

Table 2. Magnetic parameters of $\text{M}_3\text{B}_2\text{O}_6$ kotoites: T_{ord} magnetic transition temperature T_N or T_{sg} , Θ is the paramagnetic Curie temperature, μ_{eff} is the effective magnetic moment per ion

		T_{ord} , K	Θ , K	μ_{eff} , μ_B/ion
$\text{Ni}_3\text{B}_2\text{O}_6$	Polycrystals [13]	49	−5	3.07
$\text{Co}_3\text{B}_2\text{O}_6$	Polycrystals [13]	30	−63	5.29
$\text{Mn}_3\text{B}_2\text{O}_6$	Polycrystals [13]	3	−185	6.18
$\text{Cu}_3\text{B}_2\text{O}_6$	Single crystals [19]	9.8	−422	1.05–1.54
$\text{Cu}_2\text{CoB}_2\text{O}_6$	Polycrystals [21]	5	−65.7	5.83
$\text{Cu}_2\text{NiB}_2\text{O}_6$	Polycrystals [23]	15	−36.8	3.44
$\text{Cu}_2\text{CdB}_2\text{O}_6$	Polycrystals [24]	9.8	−47.4	—

the symmetry decreases to triclinic one [19, 20]. Partial substitution of ion $\text{M}'^{2+} = \text{Co}, \text{Ni}, \text{ or } \text{Cd}$ for the Cu^{2+} ion causes a transition into the monoclinic phase [21–24].

The magnetic studies [13] of homometallic $\text{Co}_3\text{B}_2\text{O}_6$, $\text{Ni}_3\text{B}_2\text{O}_6$, and $\text{Mn}_3\text{B}_2\text{O}_6$ compounds showed that they undergo a transition into an antiferromagnetic state with the formation of a long-range magnetic order (Table 2). The effective magnetic moments are typical of divalent Co, Ni, and Mn ions. The magnetic structures of $\text{Co}_3\text{B}_2\text{O}_6$ and $\text{Ni}_3\text{B}_2\text{O}_6$ were investigated by neutron diffraction at temperatures above and below the magnetic transition temperature [13, 25]. A low-temperature model implies the existence of a $2a \times b \times 2c^*$ magnetic supercell, which is larger than

the crystallographic unit cell by four times. The authors of [13, 25] assumed the presence of a spin configuration in which the magnetic moments of cobalt ions ordered ferromagnetically along axis b are normal to axis a .

The magnetic studies of copper oxyborates $\text{Cu}_{3-x}\text{M}'_x\text{B}_2\text{O}_6$ ($\text{M}' = \text{Co}, \text{Ni}, \text{Cd}; x = 0.0, 1.0$) are more comprehensive. A combined investigation of the magnetic, caloric, and resonance properties and the measurements of neutron scattering and spin relaxation showed that a complex magnetic structure, which includes both interacting single spins (singlet phase) and clusters made of several spins (magnetically ordered phase), forms in $\text{Cu}_3\text{B}_2\text{O}_6$. A transition into the state that is the superposition of these two

phases takes place at temperatures below 10 K [20, 26]. Interestingly, the isostructural $\text{Cu}_2\text{CoB}_2\text{O}_6$ and $\text{Cu}_2\text{NiB}_2\text{O}_6$ compounds demonstrate fully different magnetic behavior. The former compound exhibits the properties of a frustrated magnetic system and undergoes a transition into the state of spin glass ($T_{\text{sf}} = 5$ K), and the latter demonstrates the properties of a magnetically ordered system below $T_{\text{N}} = 15$ K. This difference in the properties is explained by a strong competition between the exchange interactions inside and between magnetic bands formed by six rows of magnetic ions $\text{Cu}-\text{Co}(\text{Ni})-\text{Cu}-\text{Cu}-\text{Co}(\text{Ni})-\text{Cu}$. The high sensitivity of the magnetic system to the type of a magnetic ion and its spatial location inside the band leads to an unstable balance of magnetic couplings.

Earlier, we comprehensively studied the crystal structure and the magnetic and transport properties of cobalt-based oxyborates with a ludwigite structure (Co_3BO_5 , $\text{Co}_{3-x}\text{Fe}_x\text{BO}_5$). The measurements of magnetization performed in various crystallographic directions allowed the authors of [27–29] to reveal a strong easy-axis magnetic crystallographic anisotropy and an extraordinary increase in the coercive field when iron was introduced into monocobalt ludwigite. Transition ions Co and Fe in ludwigites have the di- and trivalent degrees of oxidation and occupy four nonequivalent crystallographic positions. In contrast to them, the cobalt ions in kotoite $\text{Co}_3\text{B}_2\text{O}_6$ are only in the divalent state (Co^{2+}) and occupy two crystallographically nonequivalent positions, which strongly simplifies the interpretation of magnetic data.

It should be noted that the majority of the magnetic studies performed to date used polycrystalline samples (see Table 2). The absence of magnetic measurements on single crystals casts doubt on the isotropy of the magnetic parameters and phase-transition temperatures with allowance for the strongly anisotropic properties of the related ludwigites. Therefore, the purpose of this work is to study the magnetic properties and the magnetic anisotropy of $\text{Co}_3\text{B}_2\text{O}_6$ single crystals.

The complex magnetic behavior of oxyborates depends substantially on the configuration of local cation–cation interactions, which, in turn, are caused by a local atomic structure. On the whole, the problem of the relation between the microstructure of solid-state oxide materials and their integral physical properties is one of the fundamental problems of the condensed-matter physics. We used X-ray absorption spectroscopy based on synchrotron radiation as the method applied to obtain necessary information on a local atomic environment. This method has a sufficient sensitivity to study the changes in a local structure on a microlevel induced by various external actions [30]. Two parts of an X-ray absorption spectrum, namely, X-ray absorption near-edge structure (XANES) and extended X-ray absorption fine structure (EXAFS), yield mutually complementary information. EXAFS makes it possible to obtain informa-

tion on interatomic distances, to estimate coordination numbers, and to determine the type of ligand [31]. XANES contain information on the electronic state of absorbing atom, namely, its valence, the density of states, and the geometry of environment (including bond angles) [32].

To the best of our knowledge, experimental XANES and EXAFS studies of transition metal oxyborates have not been performed to date. Moreover, there are no theoretical and experimental works dealing with the local atomic structure of these materials and its evolution induced by an external action. Therefore, to study the local atomic structure of a $\text{Co}_3\text{B}_2\text{O}_6$ single crystal above and below the magnetic transition temperature is of particular interest.

2. SYNTHESIS OF SINGLE CRYSTALS AND X-RAY DIFFRACTION

Single-crystal kotoite $\text{Co}_3\text{B}_2\text{O}_6$ samples were grown by the flux method from a solution, namely, a melt of 55 wt % ($\text{Bi}_2\text{Mo}_3\text{O}_{12} + 2.1\text{B}_2\text{O}_3 + 0.7\text{Li}_2\text{O}$) + 45 wt % $\text{Co}_3\text{B}_2\text{O}_6$, prepared in a platinum crucible. After 4-h homogenization at $T = 1100^\circ\text{C}$, the molten solution was rapidly cooled to $T = 980^\circ\text{C}$ and the temperature was then lowered at a rate of $4^\circ\text{C}/\text{day}$. The crystal growth lasted approximately three days. The grown samples were dark crimson, had the shape of oblique prisms, and were optically transparent. The crystal sizes were $1.2 \times 5.0 \times 23.0$ mm³.

The crystal structure of the samples was studied with a Bruker SMART APEX II single-crystal X-ray diffractometer at room temperature (CCD detector) using MoK_α radiation and the SHELXTL software package [33]. The measurements showed that the crystal structure of $\text{Co}_3\text{B}_2\text{O}_6$ belongs to the orthorhombic crystal system (space group $Pnmm$). The unit cell parameters are given in Table 3 and are in good agreement with the data in [15]. The calculated density of $\text{Co}_3\text{B}_2\text{O}_6$ is 2.51 g/cm³. The atomic coordinates and the thermal parameters are given in Table 4.

In the structure of kotoite, $3d$ cations located in the octahedral environment of oxygen are situated along crystallographic axis b . Co atoms occupy two crystallographically nonequivalent positions, Co1 ($2a$) and Co2 ($4f$). Oxygen atoms also have two positions, O1 and O2. A boron atom is surrounded by three oxygen atoms and forms planar triangular anion $(\text{BO}_3)^{3-}$. Each $(\text{BO}_3)^{3-}$ anion connects several CoO_6 octahedra. The interatomic distances determined from X-ray diffraction (XRD) data are given in Table 5. The average B–O distance and the B–O–B bond angle are 1.386 Å and 119.92° , which agrees well with the trigonal symmetry of the BO_3 group. The Co–O distance falls in the range 2.073 – 2.126 Å for ion Co1 and 2.067 – 2.169 Å for ion Co2. The O–Co1/Co2–O bond angles are in the range 66.66° – 113.34° for Co1 and 81.56° – 105.50° for Co2. The octahedra have different degrees of distortion. The octahedron around Co1 is com-

Table 3. XRD data for Co₃B₂O₆

Chemical formula	Co ₃ B ₂ O ₆
Wavelength, Å	0.71073
Crystal sizes, mm ³	0.37 × 0.22 × 0.03
Temperature, K	296
Crystal structure	Orthorhombic
Space group	<i>Pnmm</i> (58)
<i>a</i> , Å	4.5287(6)
<i>b</i> , Å	5.4614(8)
<i>c</i> , Å	8.4391(12)
$\alpha = \beta = \gamma$	90.000°
<i>V</i> , Å ³	208.72(5)
<i>Z</i>	2
Density (calculated), g/cm ³	2.50771
Absorption coefficient, mm ⁻¹	5.867
<i>F</i> (000)	148
Θ	4.45°–29.39°
Correction	Gaussian
Fitting method	Least squares method
Goodness of fit	1.039
Index R1	0.0286
Index wR2	0.0449

pressed, and the octahedron around Co2 is extended (orthorhombic distortion is present along with tetragonal one).

Similarly to warwickites and ludwigites, it is convenient to represent the crystal structure of kotoite in the form of structural units connected to each other to form a volumetric skeleton and propagating along the preferred direction. The cobalt atoms in positions 2–1–2 are joined to form triangles, which are connected by vertex Co1 with each other, propagate along crystallographic axis *b*, and form infinite chains (Fig. 1). Co1 ions belong to two neighboring triangles simultaneously. The interionic distances inside the Co1–Co2 and Co2–Co2 triangle chains are almost the same, 3.151 and 3.146 Å, respectively. The minimum distance between the chains is 3.48 Å and corresponds to the Co1–Co2 distance.

3. XANES AND EXAFS SPECTROSCOPY

The X-ray spectra of the *K*-edge absorption of cobalt (EXAFS and XANES spectra) were recorded at the Structural Materials Science Station (Sibir⁻² storage ring), the Russian Research Centre Kurchatov Institute, at 2.5 GeV and an average electron current of 80 mA. The absorption spectra were recorded in transmission geometry, and a silicon single crystal with a Si(111) slit, which provided an energy resolution $\Delta E/E \approx 2 \times 10^{-4}$, was used as a monochromator. The incident and transmitted radiation intensities were detected with ionization chambers filled with air and connected to Keithley-6487 digital picoammetermeters. The scanning step in the XANES region was about 0.5 eV, and scanning in the EXAFS region was carried out at a constant step on the scale of the moduli of photoelectron wavevectors with $\Delta k = 0.05 \text{ \AA}^{-1}$, and the signal accumulation time per point was 4 s.

To study EXAFS and XANES spectra, we prepared a dark brown powder from the Co₃B₂O₆ single crystals and applied it onto a thin kapton film covered with a sticky layer in order to achieve uniform absorption. The spectra were measured at room temperature and at low temperatures (*T* = 10, 30, 40 K) using a closed-type Sumitomo Heavy Industries (Japan) helium cryogenic refrigerator.

The extended fine structure of X-ray absorption spectra represents the oscillations of X-ray absorption coefficient $\mu(E)$ (*E* is the X-ray photon energy) that appear as a result of the interference of the primary photoelectron waves emitted by an absorbing atom and the waves reflected by the atoms in the nearest environment. The oscillating part of $\mu(E)$ normalized by atomic absorption is described by the interference EXAFS function [34]

$$\chi(k) = \sum_j \frac{N_j S_0^2}{k} f_j(k) \quad (1)$$

$$\times \text{Im} \left\langle \frac{1}{r_j^2} \exp\left(-\frac{2r_j}{\lambda} + 2ikr_j\right) \right\rangle \exp(i\delta_j(k)),$$

where *k* is the photoelectron wavevector specified by the relation $k = (0.2625(E - E_0))^{1/2}$ (*E*₀ is the absorption *K*-edge energy), *f_i* is the amplitude of the probability of 180° photoelectron scattering (backscattering amplitude), *N_j* is the number of atoms in the *j*th coord-

Table 4. Atomic coordinates (×10⁴) and thermal parameters (Å² × 10⁴) for Co₃B₂O₆

	<i>x</i>	<i>y</i>	<i>z</i>	<i>U</i> ₁₁	<i>U</i> ₂₂	<i>U</i> ₃₃	<i>U</i> ₁₂	<i>U</i> ₁₃	<i>U</i> ₂₃
Co1	0	0	0	79.4	56.4	97.4	−3.3	0	0
Co2	0	5000	1864.25	91.3	71.3	66.3	−2.617	0	0
O1	3019.4	2076.3	1384.2	111.8	122.9	102.8	−4.7	5.7	10.7
O2	2476.5	−3192.4	0	101.13	103.13	114.11	1.1	0	0
B	−4593.9	7457.7	0	122	54.19	132.19	18.14	0	0

Table 5. Bond lengths, bond angles, sum of valence bonds, and distortion index for $\text{Co}_3\text{B}_2\text{O}_6$

Cobalt coordination			
Co1–O1	2.1258(17) Å	Co2–O2i	2.1695(17) Å
Co1–O2v	2.0728(22) Å	Co2–O1ii	2.0678(17) Å
Co1–O1v	2.1258(17) Å	Co2–O1iii	2.1409(17) Å
Co1–O1ix	2.1258(17) Å	Co2–O2iv	2.0678(17) Å
Co1–O2	2.0728(2) Å	Co2–O2v	2.1696(16) Å
Co1–O1vi	2.1258(17) Å	Co2–O1	2.1409(17) Å
O1–Co1–O2v	84.224(45)°	O1iv–Co2–O1	105.50(4)°
O2–Co1–O1	95.78(7)°	O1ii–Co2–O1iv	88.72(10)°
O2–Co1–O1ix	84.22(7)°	O1iv–Co2–O1	90.20(4)°
O1ix–Co1–O2v	95.776(45)°	O1iv–Co2–O2v	92.559(49)°
O1v–Co1–O2v	95.776(45)°	O1ii–Co2–O1iii	90.20(4)°
O1–Co1–O1v	113.34(9)°	O1ii–Co2–O1	105.50(4)°
O2–Co1–O1v	84.22(7)°	O1–Co2–O2v	81.566(45)°
O1ix–Co1–O1v	66.66(9)°	O1iii–Co2–O2v	82.656(46)°
O1vi–Co1–O2v	84.224(45)°	O1iii–Co2–O2i	81.56(8)°
O1–Co1–O1vi	66.66(9)°	O1ii–Co2–O2i	92.57(7)°
O2–Co1–O1vi	95.78(7)°	O1–Co2–O2i	82.66(7)°
O1ix–Co1–O1vi	113.34(9)°	O2i–Co2–O2v	87.045(3)°
O1vi–Co1–O1v	180.00(11)°	O1ii–Co2–O2v	172.823(47)°
O2v–Co1–O2	180.000(86)°	O1iii–Co2–O1	158.18(9)°
O1–Co1–O1ix	180.000°	O1iv–Co2–O2i	172.83(8)°
Boron coordination			
B–O1	1.3919(28) Å	O1–B–O1vi	114.1(3)°
B–O1vi	1.392(3) Å	O1vi–B–O2vii	122.83(16)°
B–O2vii	1.374(4) Å	O2vii–B–O1	122.83(16)°
Distortion index			
(Co1)O ₆	0.011		
(Co2)O ₆	0.018		

Note: Symmetry codes: (i) $x, 1 + y, z$; (ii) $0.5 - x, 0.5 + y, 0.5 - z$; (iii) $-x, 1 - y, z$; (iv) $-0.5 + x, 0.5 - y, 0.5 - z$; (v) $-x, -y, z$; (vi) $x, y, -z$; (vii) $1 - x, -y, z$; (viii) $x/a, y/b, z/c$; (ix) $-x, -y, -z$.

dination shell, $\delta_j(k)$ is the phase shift in reflection, r_j is the current position of an atom in the j th shell with respect to the absorbing atom, λ is the photoelectron free path length, and S_0^2 is the probability of the one-electron processes forming EXAFS during photon absorption. The angle parentheses mean averaging over the thermal atom deviations from an equilibrium position.

The oscillating part of the absorption coefficient normalized by atomic absorption is [36]

$$\chi(k) = \frac{\mu(k) - \mu_0(k)}{\mu_0(k) - \mu_1(k)}, \quad (2)$$

where $\mu(k)$ is the experimental absorption coefficient of the sample, $\mu_1(k)$ is the absorption coefficient

caused by all processes except for the photoionization of the electron shell of the atom, and $\mu_0(k)$ is the absorption coefficient that would be expected in the absence of neighboring atoms near the absorbing atom.

After the standard procedures of background separation, normalization by the K -edge jump, and the separation of atomic absorption μ_0 [35], we performed the Fourier transform of the recorded EXAFS spectra (χ_{exp}) in the photoelectron wavevector range $k = 2.0 - 14.5 \text{ \AA}^{-1}$ with weighting function k^3 using the Kaiser–Bessel window. Threshold ionization energy E_0 was chosen from the maximum of the first derivative of the K edge. The exact parameters of the structure of the nearest environment of cobalt atoms were determined

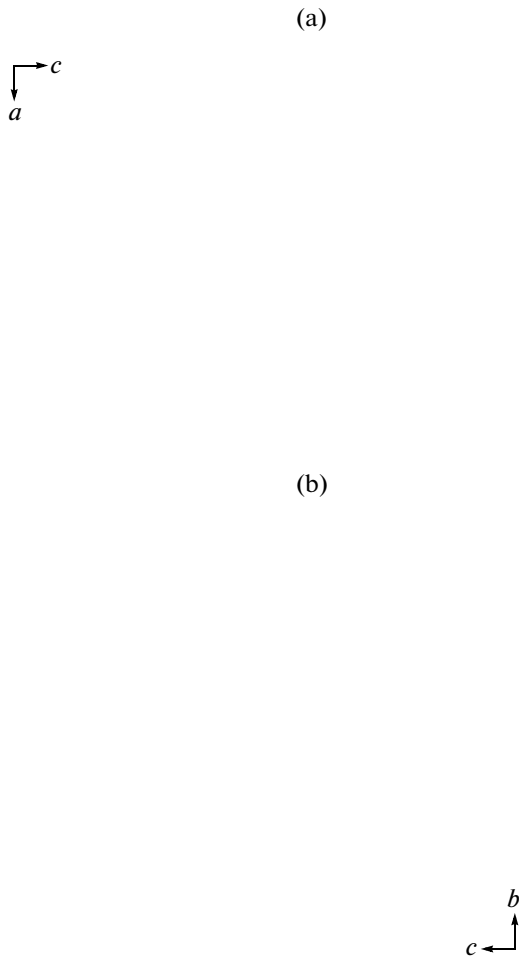


Fig. 1. Crystal structure of kotoite $\text{Co}_3\text{B}_2\text{O}_6$ as the projection on plane (a) ac and (b) bc : (big open and solid circles) cobalt ions in positions 1 and 2, respectively; (medium circles) boron ions; and (small circles) oxygen ions. The rectangle indicates the unit cell.

by nonlinear fitting of the parameters of the corresponding coordination shells. To this end, we compared a calculated EXAFS signal and the moduli of the Fourier transform separated from the entire EXAFS spectrum. This procedure of nonlinear fitting was performed using the IFFEFIT software package [36]. The photoelectron wave phases and amplitudes required for constructing a theoretical spectrum were calculated by the FEFF8 software package [37]. The initial approximations for the parameters of the local environment of cobalt were chosen on the basis of XRD data.

As standards for an analysis of the XANES spectra, we used the spectra of oxides CoO (Co^{2+}) and Co_2O_3 (Co^{3+}).

Figure 2 shows the XANES spectra of $\text{Co}_3\text{B}_2\text{O}_6$ at the K edge of cobalt in the energy range 7700–7760 eV at various temperatures. For comparison, we also show the spectra of model compounds CoO and Co_2O_3

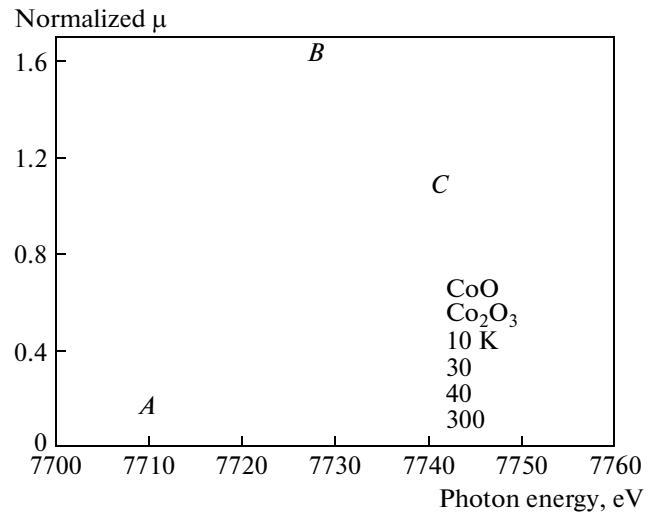


Fig. 2. Normalized XANES spectra of $\text{Co}_3\text{B}_2\text{O}_6$ as compared to the spectra of CoO (Co^{2+}) and Co_2O_3 (Co^{3+}).

recorded at room temperature. The coincident maxima of the first derivative of the K -edge absorption for CaO and $\text{Co}_3\text{B}_2\text{O}_6$ indicate that the compound under study contains cobalt only in the divalent state (Fig. 3). This conclusion is fully consistent with the results of calculation by the valence sum method.

The specific features indicated by letters A , B , and C in Fig. 2 can be distinguished in the absorption edge region, and they can be interpreted as the transitions of a photoelectron excited from the $1s$ level of cobalt to bound states and as the processes of its scattering by the local environment. Feature A , which is located before the fundamental absorption edge, corresponds to the quadrupole $1s-3d$ transition for octahedral environment [38]. Although the intensity of the near-edge transition is usually very low, this transition can be experimentally detected due to a high density of states in the $3d$ band and the hybridization of the $3d-4p$ bands. The main absorption maximum B corresponds to the dipole-allowed $1s-4p$ transition. In the multiple scattering formalism, maximum C corresponds to resonance photoelectron scattering by the oxygen atoms in the first coordination shell. The specific features of the fine structure that have higher energies exhibit EXAFS nature.

It is very difficult to perform a full quantitative analysis of EXAFS spectra because of the complex crystal structure of the oxyborates. Therefore, the analysis of the recorded spectra was restricted to the first coordination shell. As is seen in Fig. 4, the moduli of the Fourier transforms of the EXAFS spectra consist of the first peak ($r \approx 1.50-2 \text{ \AA}$), which corresponds to $\text{Co}-\text{O}$ coordination shell, the second peak ($r \approx 2.50-3.2 \text{ \AA}$), which corresponds to the $\text{Co}-\text{Co}$ coordination shell, and low-intensity peaks, which correspond to multiple scattering effects and the $\text{Co}-\text{B}$ dis-

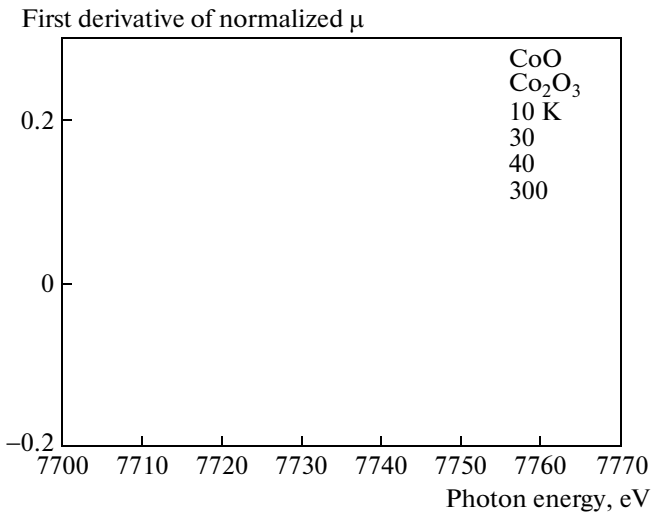


Fig. 3. First derivative of the normalized XANES spectra of $\text{Co}_3\text{B}_2\text{O}_6$ at a temperature of 10, 30, 40, and 300 K in comparison with the spectra of Co^{2+} and Co^{3+} .

tances. The high-intensity Fourier transform peak ($r \approx 5.1 \text{ \AA}$) corresponds to the Co–Co distances (5.45–5.55 \AA). The structure of $\text{Co}_3\text{B}_2\text{O}_6$ has 18 Co–Co contacts in this distance range. The high intensity of this peak, which is observed even at room temperature, points to the rigidity of the chemical bonds that form this structure. As the temperature decreases, the intensity of the Co–Co peaks in Fourier transforms increases substantially according to the decrease in the average thermal vibration amplitude (Debye–Waller

parameter). The temperature changes for the first coordination shell are nonmonotonic: the maximum peak intensity is observed at $T = 40 \text{ K}$, and the intensity decreases upon the subsequent decrease in the temperature. This change is systematic and exceeds the statistical measurement error in absolute value.

The maximum intensity of the Co–O peak in the Fourier transform at a temperature of 40 K (near the magnetic phase transition) corresponds to the point of maximum effective ordering, which takes into account both the dynamic component (thermal vibration amplitude) and the static component (structure-induced scatter of the bond lengths).

A quantitative analysis was carried out for the first Fourier transform maximum in the distance range $r = 1.0\text{--}2.2 \text{ \AA}$ and the photoelectron wavevector range $k = 2.0\text{--}14.5 \text{ \AA}^{-1}$. According to the XRD data, the nearest Co–O distances can be divided into two groups with an average value of $\langle (\text{Co1-O})_1 \rangle = 2.07 \text{ \AA}$ (two bonds, $N = 2$) and $\langle (\text{Co1-O})_2 \rangle = 2.12 \text{ \AA}$ (four bonds, $N = 4$) for the cobalt ions in position 1. Similarly, for Co2 we have $\langle (\text{Co2-O})_1 \rangle = 2.07 \text{ \AA}$ ($N = 2$) and $\langle (\text{Co2-O})_2 \rangle = 2.15 \text{ \AA}$ ($N = 4$). The average distance $\langle \text{Co-O} \rangle$ ($N = 6$) in the crystal is close to 2.11 \AA .

An analysis was performed in terms of both one- and two-shell structural models, which included either one averaged distance $\langle \text{Co-O} \rangle$ ($N = 6$) or distances $(\text{Co-O})_1$ and $(\text{Co-O})_2$ with coordination numbers 2 and 4, respectively. We calculated EXAFS functions $\chi_{\text{theor}}(k)$ and fitted the parameters of the first Fourier transform peak. Table 6 gives the parameters of the

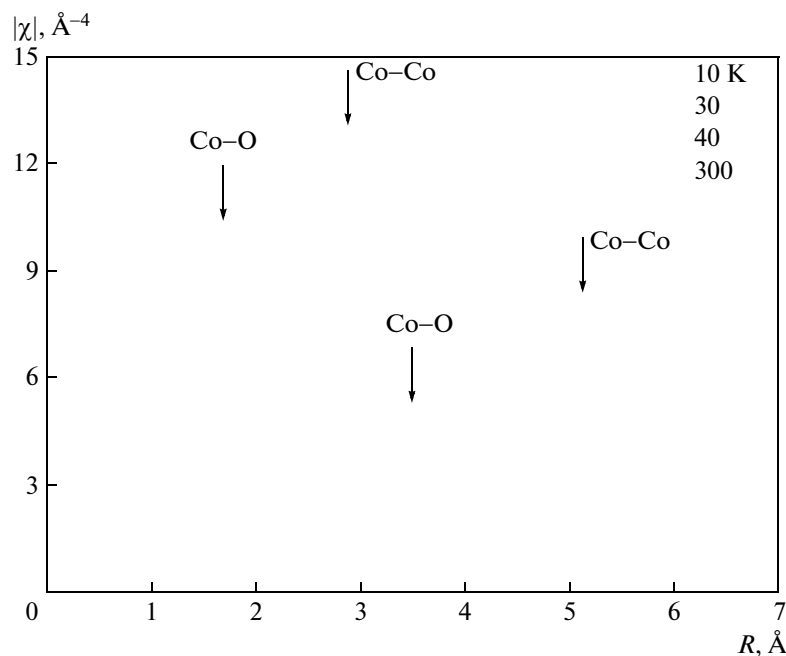


Fig. 4. Fourier transform separated from the EXAFS spectra of $\text{Co}_3\text{B}_2\text{O}_6$ at various temperatures.

local environment of cobalt obtained upon the best fitting of EXAFS data. The one-shell model well describes the experimental EXAFS spectra. The average $\langle\text{Co-O}\rangle$ bond weakly changes with temperature and is close to 2.10 Å, which is in good agreement with the XRD data obtained at room temperature. In this case, the effective Debye parameters pass through a minimum at $T = 40$ K. The use of two nonequivalent Co–O distances with coordination numbers 2 and 4 in the refined model improves the convergence of the spectrum measured at $T = 10$ K. The following distances of two types can be distinguished in terms of this model: “short” distances $(\text{Co-O})_1 = 2.02\text{--}2.09$ Å and “long” distances $(\text{Co-O})_2 = 2.11\text{--}2.13$ Å. These distances change differently with temperature. The former distance increases with temperature and the later exhibits a small decrease. In terms of the two-shell refinement, the change in the Debye parameters with decreasing temperature is characterized by a monotonic decrease.

4. MAGNETIZATION AND MAGNETIC SUSCEPTIBILITY

The magnetic properties of $\text{Co}_3\text{B}_2\text{O}_6$ were studied with commercial SQUID MPMS and PPMS Quantum Design platforms in the temperature range $T = 2\text{--}300$ K on a single crystal when a magnetic field was applied parallel (M_{\parallel}) and normal (M_{\perp}) to axis a of the crystal.

Figure 5 shows the real component of magnetization $M'(T)$ detected in an ac applied magnetic field ($f = 0.1\text{--}10$ kHz) at various orientations of a dc applied magnetic field with respect to crystallographic axis a . In both cases, the $M'(T)$ dependence has two maxima, the first of which corresponds to the transition of the sample into an antiferromagnetic state with temperature ($T_1 = 33$ K). It should be noted that transition temperature T_1 is in good agreement with the magnetic data ($T_N = 30\text{--}37$ K) in [13, 25, 39]. When the temperature decreases further, a weak specific feature is visible at $T_2 = 10$ K. The sample does not exhibit dispersion of the critical temperatures (T_1, T_2) in an ac magnetic field. The measurements performed under various cooling conditions (FC, ZFC) did not reveal differences in the magnetization curves (not presented here). It is seen that the field direction is parallel to crystallographic axis a , which is an easy magnetization axis.

The anisotropy of magnetization is also visible in the temperature dependences of the reciprocal magnetic susceptibility in a dc magnetic field (inset to Fig. 5). The Curie–Weiss law holds true over a wide temperature range from the side of high temperatures. The paramagnetic Curie temperatures are $\Theta_{\perp} = -115$ K and $\Theta_{\parallel} = -52$ K. The negative values of these temperatures indicate predominantly antiferromagnetic spin correlations. The effective magnetic

Table 6. Parameters of the nearest environment of cobalt obtained by fitting EXAFS data in terms of one- and two-shell models

T , K	Scattering path	r , Å	N	σ^2 , Å ²	E_0 , eV	R factor
10	$\langle\text{Co-O}\rangle$	2.11	6	0.0058	0.1	0.008
	$(\text{Co-O})_1$	2.02	2	0.0025	-1.4	0.003
	$(\text{Co-O})_2$	2.13	4			
30	$\langle\text{Co-O}\rangle$	2.10	6	0.0055	-0.4	0.007
	$(\text{Co-O})_1$	2.03	2	0.0032	-1.2	0.006
	$(\text{Co-O})_2$	2.12	4			
40	$\langle\text{Co-O}\rangle$	2.10	6	0.0054	0.3	0.011
	$(\text{Co-O})_1$	2.06	2	0.0047	0.3	0.011
	$(\text{Co-O})_2$	2.12	4			
300	$\langle\text{Co-O}\rangle$	2.10	6	0.0074	0.0	0.020
	$(\text{Co-O})_1$	2.09	2	0.0074	0.0	0.020
	$(\text{Co-O})_2$	2.11	4			

Note: r is the interatomic distance, N is the coordination number, σ^2 is the Debye–Waller factor, E_0 is the atom ionization threshold, and R factor is the deviation of $\chi_{\text{theor}}(k)$ from $\chi_{\text{exp}}(k)$.

moment per Co^{2+} ion is $\mu_{\text{eff}\parallel} = 4.81\mu_B$ and $\mu_{\text{eff}\perp} = 4.98\mu_B$ for the parallel and perpendicular magnetic-field orientation, respectively.

Figure 6 shows the temperature dependences of magnetization measured in a magnetic field up to 50 kOe that is parallel to axis a . The experimental magnetic moment measured at $T = 4.2$ K in a field of 10 kOe is close to the value found in [25, 39]. As the magnetic field increases, the low-temperature maximum shifts slightly toward low temperatures, in contrast to the transition at T_1 (which is field-independent). It is rather difficult to find the field dependence of T_2 from the experimental $M(T)$ curves. This dependence can be more accurately revealed from the temperature dependence of the $dM/dT(T)$ derivative (inset to Fig. 6). It is seen that, as the magnetic field increases, transition temperature T_2 decreases rapidly and reaches 4 K at $H = 24$ kOe.

Figure 7 shows the isotherms of magnetization of $\text{Co}_3\text{B}_2\text{O}_6$ at $T = 2$ K and two magnetic-field orientations with respect to axis a . Both curves are seen to exhibit a specific feature, which can be related to a spin-flop transition, near $H_{\text{sf}} = 23$ kOe. The absence of a magnetic hysteresis at point H_{sf} indicates the reversibility of this transition. This feature is clearly visible in the field dependence of the $dM/dH(H)$ derivative in the form of a maximum at H_{sf} (lower inset to Fig. 7). As the temperature increases, the maximum broadens significantly and the transition becomes smoothed; nevertheless, it can be detected down to a temperature

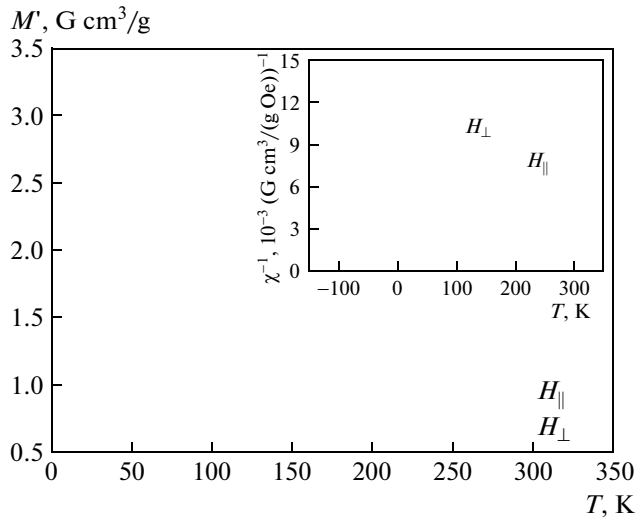


Fig. 5. Real component of the magnetization of $\text{Co}_3\text{B}_2\text{O}_6$ in an ac magnetic field ($f = 0.1, 0.5, 1.0, 5.0, 10.0$ kHz) and a dc magnetic field $H_{\parallel} = 10$ Oe. (inset) Temperature dependence of the reciprocal magnetic susceptibility of $\text{Co}_3\text{B}_2\text{O}_6$ at $H_{\parallel} = 500$ Oe. (straight line) Curie–Weiss law approximation.

of 10 K. In fields higher than H_{sf} , the magnetization curves exhibit the presence of a spontaneous magnetic moment and the magnetization can be described by the expression $M = M_0 + \chi_{\perp}H$. At $T = 2$ K, we have $M_0 = 0.11\mu_{\text{B}}$ per formula unit. As the temperature increases, M_0 decreases (upper inset to Fig. 7). At $T = 20$ K or above, the magnetization curves are linear and have no specific features. The magnetic susceptibility in the antiferromagnetic phase is $\chi_{\parallel} = 1.47 \times 10^{-5} \mu_{\text{B}}/\text{Oe}$ and $\chi_{\perp} = 0.87 \times 10^{-5} \mu_{\text{B}}/\text{Oe}$ per formula unit in a magnetic field that is parallel and perpendicular to axis a , respectively. In the range $T \geq 40$ K, the $M(H)$ curves are linear and correspond to paramagnetic behavior.

5. ANALYSIS OF EXCHANGE INTERACTIONS

We now analyze the exchange interactions in terms of a simple indirect-bond model. The theoretical fundamentals of this model were described in [40, 41]. The practical application of this model to the $3d$ cations in magnetodielectrics was shown in [42]. In [28], we performed a similar calculation for $\text{Co}_{3-x}\text{Fe}_x\text{BO}_5$ ludwigites and achieved good agreement with experimental data.

In the calculations, we restricted ourselves to the nearest-neighbor approximation; that is, we considered the interaction only along the short Co–O–Co bonds, neglecting the long Co–O–Co–O–Co and Co–O–B–O–Co bonds. From the standpoint of an indirect exchange coupling, the kotoite structure has the following four types of exchange interactions: 93° ,

95° , 112° , and 123° . They are described by the integrals

$$\begin{aligned}
 J1 &= J_{12}^{95^\circ} = -\frac{1}{9}c \left[\left(\frac{8}{3}b + c \right) U \right. \\
 &\quad \left. - \left(4b + \frac{1}{2}c \right) J_{\text{in}} \right] \approx -2.16 \text{ K}, \\
 J2 &= J_{12}^{112^\circ} = -\frac{1}{27}bc(4U - J_{\text{in}})(1 + 2\cos 65^\circ) \\
 &\quad \times |\cos 112^\circ| \approx -1.2 \text{ K}, \\
 J3 &= J_{22}^{93^\circ} = -\frac{32}{27}bcU \approx -15.44 \text{ K}, \\
 J4 &= J_{22}^{123^\circ} = -\frac{1}{9} \left(\frac{32}{9}b^2U - c^2J_{\text{in}} \right) \\
 &\quad \times |\cos 123^\circ| \approx -5.44 \text{ K}.
 \end{aligned} \tag{3}$$

Here, the superscripts mean the indirect bond angles; the subscripts mean the crystallographic position numbers; b and c are the parameters of electron transport along the σ and π bonds, respectively; U is the electron ligand–cation exchange energy; and J_{in} is the intraatomic exchange integral (Hund energy). $\cos 65^\circ$ describes the angular dependence of electron transport when the coordination octahedron rotates about its principal axis, and $|\cos 112^\circ|$ and $|\cos 123^\circ|$ take into account the indirect bond angles. The cation–cation interaction integral is the sum of the interactions of individual $3d$ orbitals.

The octahedra of the neighboring cations that have common edges cause the exchange coupling with an angle of 95° ($J1$) and the coupling with an angle of 93° ($J3$). The octahedra connected by a common oxygen atom allow an indirect coupling at an angle of 112° ($J2$) and a coupling at an angle of 123° ($J4$) (Fig. 8). As an example, we consider the contribution of cation–cation exchange interaction $J1$ to the integral. Cation Co1 is located in a compressed oxygen octahedron; as a result, according to the crystal field theory, its d_{xy} orbital is doubly occupied. The seventh electron populates the d_{xz} and d_{yz} orbitals at the same probability, and each of these orbitals can be populated either singly or doubly ($1/2(\uparrow + \uparrow\downarrow)$). The octahedron around site Co2 is elongated; therefore, the d_{xz} and d_{yz} orbitals are occupied doubly and the d_{xy} orbital is occupied singly. Local z axes were taken to be the short axis of octahedron Co1O₆ and the long axis of octahedron Co2O₆. Knowing the local axes, the shapes of $3d$ orbitals, their population for each cation, and the geometry of the relative position of neighboring octahedra, we determine the symmetry-allowed overlapping of the orbitals of interacting cations. Figure 9a shows the configurations of the individual $3d$ orbitals for the indirect Co1–Co2 coupling with an angle of 95° through two oxygen atoms and for lattice symmetry-allowed electron transport and expressions for the exchange integrals of

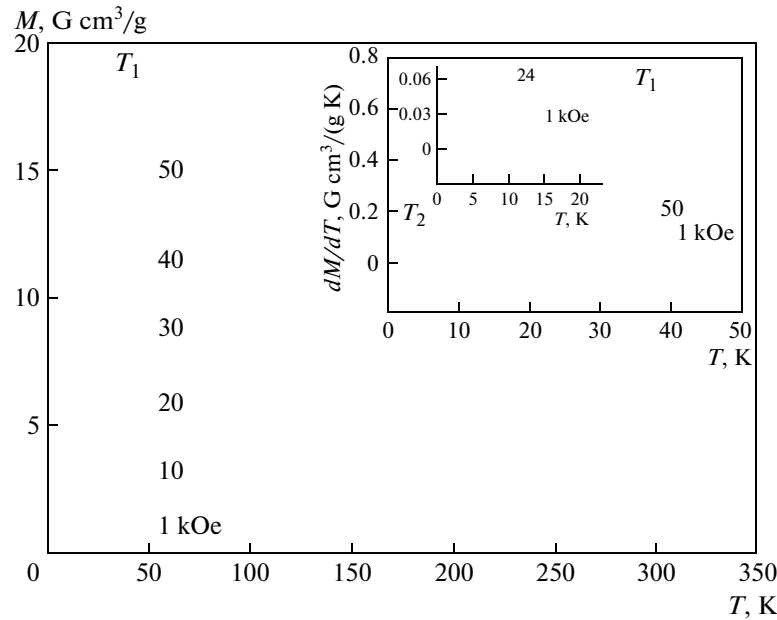


Fig. 6. Temperature dependences of the magnetization of $\text{Co}_3\text{B}_2\text{O}_6$ measured in the magnetic field range $H_{\parallel} = 1\text{--}50$ kOe. (inset) Temperature dependences of derivative dM/dT . The maxima correspond to critical transition temperatures T_1 and T_2 . The temperature-induced shift in transition temperature T_2 is enlarged.

the individual orbitals. The exchange integrals are seen to consist of both positive and negative contributions. Using the well-known parameters for a spinel structure ($b = 0.02$, $c = 0.01$, $U = 5.6$ eV, $J_{\text{in}} = 2.2$ eV [42]), the octahedral positions in which have interionic distances comparable with those in kotoite, we arrive at the estimated parameters of the cation–cation exchange interaction given in the right-hand side of Eq. (3).

The weakest interactions are represented by interactions J_1 and J_2 , which predominantly have an antiferromagnetic character. However, they are weakened by the ferromagnetic interactions induced by the overlapping of the singly occupied e_g (Co1) orbitals and the doubly occupied t_{2g} (Co2) orbitals. The strongest interactions are represented by antiferromagnetic interactions J_3 and J_4 , which correspond to the Co2–Co2 exchange coupling. In the case of the Co2–Co2 interaction at an angle of 93° , the overlapping of the singly occupied d_{z^2} , $d_{x^2-y^2}$, and d_{xy} orbitals is such that strong antiferromagnetic coupling J_3 appears (Fig. 9b). When Co2–Co2 cations are located at an angle of 123° , the antiferromagnetic interaction is weaker because of the overlapping of singly and doubly occupied orbitals $d_{xy}(\uparrow) - d_{yz}(\uparrow\downarrow)$ and singly occupied orbitals $d_{z^2}(\uparrow) - d_{z^2}(\uparrow)$ and $d_{x^2-y^2}(\uparrow) - d_{x^2-y^2}(\uparrow)$.

The interactions between all crystallographic positions are negative, which points to a tendency toward antiferromagnetic ordering. In this case, the crystallographic positions are divided into magnetic sublattices. Let kotoite be a magnet consisting of six sublattices

in which crystallographic positions Co1 are divided into two magnetic sublattices (1, 2) and crystallographic positions Co2 are divided into four magnetic sublattices (3, 4, 5, 6). The belonging of the kotoite positions to the sublattices is shown in Fig. 9. It should be noted that the indirect coupling method was applied earlier to calculate the magnetic structure of $\text{Ni}_3\text{B}_2\text{O}_6$ and $\text{Co}_3\text{B}_2\text{O}_6$ grown in a molten solution containing Na_2O . The interaction integrals obtained in this work agree well with the data in [39].

Allowing for the numbers of neighbors, we arrive at the sublattice–sublattice interactions presented in Table 7. The arrows indicate the magnetic structures (mutual orientation of magnetic moments) caused by the calculated exchange interaction parameters. The strong antiferromagnetic interactions operating in crystallographic sublattice Co2 make kotoite antiferromagnetic. The cations of sublattices 1 and 2 undergo both ordering interactions, which support the antiferromagnetic structure of kotoite, and disordering interactions from the cations of sublattices 3–6. The disordering interactions are italicized in the table. In this case, the ordering interaction force is equal to that of the disordering interactions. Thus, the exchange fields at cations 1 and 2 are zero, and the magnetic moments of these sublattices are free in their behavior. Apparently, they can give a paramagnetic contribution to the magnetization of the crystal or can be randomly ordered under the action of weaker interactions or lattice defects.

Given a set of exchange interactions in the crystal, we can calculate the magnetic ordering temperature; it

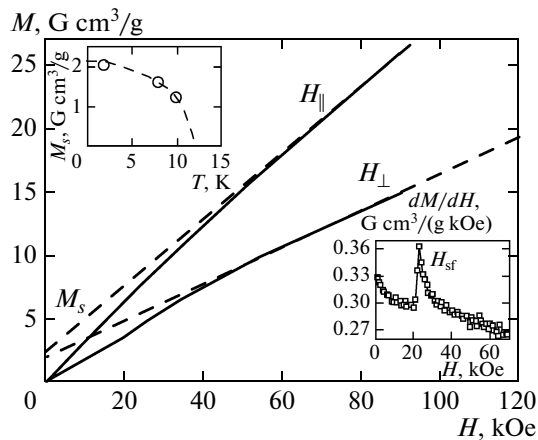


Fig. 7. Field dependences of the magnetization of $\text{Co}_3\text{B}_2\text{O}_6$ obtained at various magnetic field orientations with respect to axis a ($T = 2$ K): (dashed lines) extrapolation to zero field. (upper inset) Temperature dependence of spontaneous magnetization. The dashed lines are drawn by eye. (lower inset) Field dependence of the field derivative of magnetization ($H \parallel a$, $T = 2$ K). Spin-flop transition at $H_{\text{sf}} = 23$ kOe.

is found to be $T_N = 32$ K, which agrees well with the experimental value. The good agreement of the calculated magnetic structure and the magnetic ordering temperature with the experimental results can count in favor of the adequacy of the estimated interactions in kotoite.

6. DISCUSSION OF THE RESULTS AND CONCLUSIONS

With EXAFS and XANES, we studied the electronic state and the local crystal structure of the cobalt ion. The presence of high-intensity peaks of far coordination shells in the modulus of the Fourier transform of the EXAFS spectrum indicates a rigid chemical bond framework in the structure. The detected specific features at the K -edge absorption correspond to the quadrupole $1s-3d$ and dipole $1s-4p$ transitions. The cobalt ions were shown to be in the divalent state. For the first Fourier transform maximum, we performed a quantitative analysis in terms of one- and two-shell structural models, which took into account six average $\langle \text{Co-O} \rangle$ distances or two types of distances $(\text{Co-O})_1$ and $(\text{Co-O})_2$ with coordination numbers of 2 and 4, respectively. The calculated EXAFS functions $\chi_{\text{theor}}(k)$ well describe the experimental spectra in both cases. The interionic distances determined in terms of both models are in good agreement with the XRD data obtained on single crystals. The temperature changes in the Co-O distances manifest themselves best of all in the two-shell model. As the temperature increases, the octahedron contracts in the direction of long oxygen bonds and elongates in the direction of short bonds.

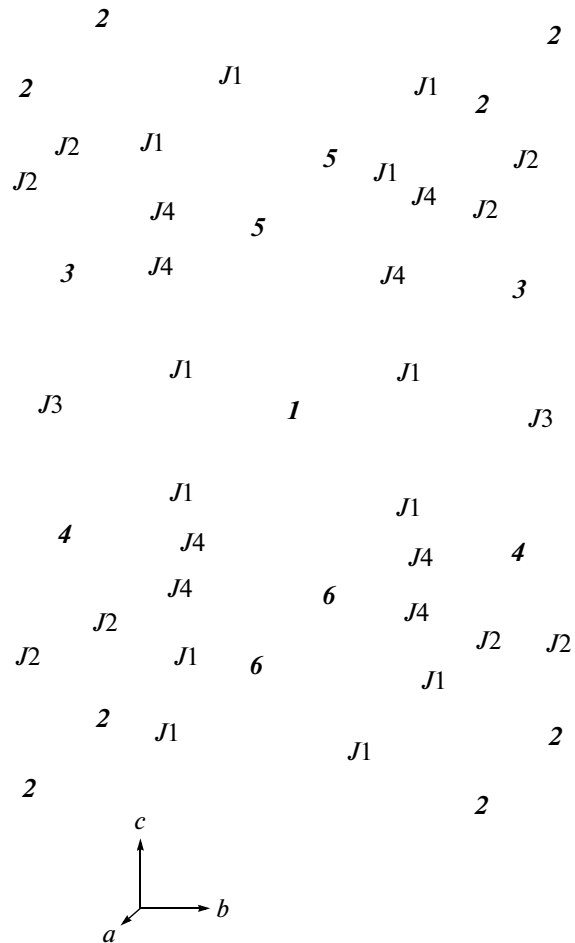


Fig. 8. Schematic diagram of indirect exchange interactions: (open circles) $\text{Co}1$ ions and (solid circles) $\text{Co}2$ ions. Numerals indicate the belonging of a crystallographic position to a magnetic sublattice.

An analysis showed a monotonic decrease in the effective Debye parameters upon cooling in both models. In the case of the one-shell approach, the Debye–Waller parameter passes through a minimum at $T = 40$ K, which can indicate changes in the local atomic structure in the magnetic phase transition region.

Magnetic measurements demonstrated that axis a is an easy magnetization axis. It is interesting that the magnetization below T_N tends toward a finite value in both directions (parallel and perpendicular to crystallographic axis a). This behavior can result from a non-collinear magnetic structure or indicate the fact that an applied magnetic field in both cases is directed at a certain angle to the antiferromagnetism axis.

The effective magnetic moments for various orientations fall in the range $\mu_{\text{eff}} = 4.81-4.98 \mu_B/\text{Co}$ and agree well with the values $(4.44-5.25 \mu_B)$ found earlier for divalent cobalt in the high-spin state ($t_{2g}^5 e_g^2$) [43].

Table 7. Integrals of intra- and intersublattice exchange interactions

$Z_{ij}J_{ij}$, K	\uparrow 1(Co1)	\downarrow 2(Co1)	\uparrow 3(Co2)	\downarrow 4(Co2)	\uparrow 5(Co2)	\downarrow 6(Co2)
\uparrow 1(Co1)	0	0	-4.32	-4.32	-2.40	-2.40
\downarrow 2(Co1)	0	0	-2.40	-2.40	-4.32	-4.32
\uparrow 3(Co2)	-4.32	-2.40	0	-15.44	-21.76	0
\downarrow 4(Co2)	-4.32	-2.40	-15.44	0	0	-21.76
\downarrow 5(Co2)	-2.40	-4.32	-21.76	0	0	-15.44
\downarrow 6(Co2)	-2.40	-4.32	0	-21.76	-15.44	0

flop transition). At $H > H_{sf}$, spin reorientation causes spontaneous magnetization, which decreases rapidly with increasing temperature.

The calculation of the exchange interactions showed that the antiferromagnetic exchange is the predominant type of exchange in $\text{Co}_3\text{B}_2\text{O}_6$, which agrees with the magnetic measurement data. Therefore, $\text{Co}_3\text{B}_2\text{O}_6$ can be considered as a three-dimensional antiferromagnet.

Figure 10 shows the magnetic phase diagram of $\text{Co}_3\text{B}_2\text{O}_6$ plotted from the results of magnetic measurements. The following three regions can be distinguished in this phase diagram: paramagnetic PM, antiferromagnetic AF1, and antiferromagnetic AF2 (where field-induced spontaneous magnetization takes place) regions. Thus, the magnetic structure of $\text{Co}_3\text{B}_2\text{O}_6$ is likely to be more complex than that assumed earlier in [25]. The existence of a spin-reorientation transition in the magnetization curves measured in two crystallographic directions indicates that

the antiferromagnetism axis is likely to be located at an angle to axes a and b .

In conclusion, we note that our anisotropic interaction calculations have an estimation character and were carried out for the case of a uniaxial antiferromagnet without regard for exchange coupling frustrations. Neutron diffraction investigations in a magnetic field are of particular interest for obtaining additional data on the magnetic phase diagram of $\text{Co}_3\text{B}_2\text{O}_6$.

ACKNOWLEDGMENTS

We thank S.N. Sofronova for useful discussions.

The synchrotron measurements were performed at the Kurchatov Center of Synchrotron Radiation and Nanotechnologies (state contract no. 16.552.11.7055).

This work was supported by the Russian Foundation for Basic Research (project nos. 12-02-00175-a, 12-02-90410-Ukr_a, 12-02-31543mol_a, 13-02-00958-a), the President of the Russian Federation (grant no. NSh-1044.2012.2), the Siberian Branch of the Russian Academy of Sciences (project no. 38), the Ministry of Education and Science of the Russian Federation (project no. 8365), and an integration project of SO RAN–NAN of Belarus (project no. 29).

REFERENCES

1. A. K. Zvezdin, S. S. Krotov, A. M. Kadomtseva, G. P. Vorob'ev, Yu. F. Popov, A. P. Pyatakov, L. N. Bezmaternykh, and E. A. Popova, JETP Lett. **81** (6), 272 (2005).
2. A. D. Balaev, L. N. Bezmaternykh, I. A. Gudim, V. L. Temerov, S. G. Ovchinnikov, and S. A. Kharlamova, J. Magn. Magn. Mater. **258–259**, 532 (2003).
3. I. A. Troyan, A. G. Gavriluk, S. G. Ovchinnikov, I. S. Lyubutin, and N. V. Kazak, JETP Lett. **94** (10), 748 (2011).

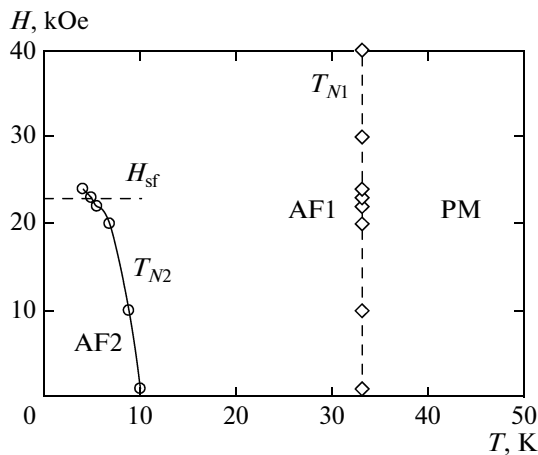


Fig. 10. Magnetic phase diagram of $\text{Co}_3\text{B}_2\text{O}_6$. The dashed line is drawn by eye.

4. A. G. Gavriluk, N. V. Kazak, S. G. Ovchinnikov, and I. S. Lyubutin, *JETP Lett.* **88** (11), 762 (2008).
5. R. Komatsu, T. Sugawara, K. Sassa, N. Sarukura, Z. Liu, S. Izumida, Y. Segawa, S. Uda, T. Fukuda, and K. Yamanouchi, *Appl. Phys. Lett.* **70**, 3492 (1997).
6. I. N. Ogorodnikov, N. E. Poryvai, V. A. Pustovarov, A. V. Tolmachev, R. P. Yavetski³, and V. Yu. Yakovlev, *Phys. Solid State* **51** (6), 1160 (2009).
7. N. B. Ivanova, A. D. Vasil'ev, D. V. Velikanov, N. V. Kazak, S. G. Ovchinnikov, G. A. Petrakovski, and V. V. Rudenko, *Phys. Solid State* **49** (4), 651 (2007).
8. J. P. Attfield, A. M. T. Bell, L. M. Rodrigues-Martinez, J. M. Greneche, R. Retoux, R. J. Cernik, J. F. Clarke, and D. A. Perkins, *J. Mater. Chem.* **9**, 205 (1999).
9. R. I. Goff, A. J. Williams, and J. P. Attfield, *Phys. Rev. B: Condens. Matter* **70**, 014426 (2004).
10. Yu. V. Knyazev, N. B. Ivanova, N. V. Kazak, M. S. Platunov, L. N. Bezmaternykh, D. A. Velikanov, A. D. Vasiliev, S. G. Ovchinnikov, and G. Yu. Yurkin, *J. Magn. Magn. Mater.* **324**, 923 (2012).
11. J. C. Fernandes, F. S. Sarrat, R. B. Guimaraes, R. S. Freitas, M. A. Continentino, A. C. Doriguetto, Y. P. Mascarenhas, J. Ellena, E. E. Castellano, J.-L. Tholence, J. Dumas, and L. Ghivelder, *Phys. Rev. B: Condens. Matter* **67**, 104413 (2003).
12. J. Pardo, M. Martinez-Ripoll, and S. Garcia-Blanco, *Acta Crystallogr., Sect. B: Struct. Crystallogr. Cryst. Chem.* **30**, 37 (1974).
13. R. E. Newnham, R. P. Santoro, P. F. Seal, and G. R. Stallings, *Phys. Status Solidi* **16**, K17 (1966).
14. H. Effenberger and F. Pertlik, *Z. Kristallogr.* **166**, 129 (1984).
15. S. V. Berger, *Acta. Chem. Scand.* **3**, 660 (1949).
16. O. S. Bondareva, M. A. Simonov, and N. B. Belov, *Sov. Phys. Crystallogr.* **23** (3), 269 (1978).
17. B. Tekin and H. Guler, *Mater. Chem. Phys.* **108**, 88 (2008).
18. H. Guler and B. Tekin, *Inorg. Mater.* **45**, 538 (2009).
19. H. Behm, *Acta Crystallogr., Sect. B: Struct. Crystallogr. Cryst. Chem.* **38**, 2781 (1982).
20. G. A. Petrakovskii, L. N. Bezmaternykh, O. A. Bayukov, K. L. Sablina, and A. M. Vorotynov, *Phys. Solid State* **41** (4), 610 (1999).
21. Zhangzhen He, Toru Kyomen, and Mitsuru Itoh, *Phys. Rev. B: Condens. Matter* **70**, 134431 (2004).
22. J. Schaefer and K. Bluhm, *Z. Anorg. Allg. Chem.* **620**, 1051 (1994).
23. Zhangzhen He, Tôru Kyômen, Tomoyasu Taniyama, and Mitsuru Itoh, *J. Solid State Chem.* **179** (12), 3937 (2006).
24. M. Hase, A. Dônni, V. Yu. Pomjakushin, L. Keller, F. Gozzo, A. Cervellino, and M. Kohno, *Phys. Rev. B: Condens. Matter* **80**, 104405 (2009).
25. R. E. Newnham, M. J. Redman, and R. P. Santor, *Z. Kristallogr.* **121**, 418 (1965).
26. M. Boehm, B. Roessli, J. Schefer, A. S. Wills, B. Oulad-diaf, E. Lelièvre-Berna, U. Staub, and G. A. Petrakovskii, *Phys. Rev. B: Condens. Matter* **68**, 024405 (2003).
27. J. Bartolomè, A. Arauzo, N. V. Kazak, N. B. Ivanova, S. G. Ovchinnikov, Yu. V. Knyazev, and I. S. Lyubutin, *Phys. Rev. B: Condens. Matter* **83**, 144426 (2011).
28. N. V. Kazak, N. B. Ivanova, O. A. Bayukov, S. G. Ovchinnikov, A. D. Vasiliev, V. V. Rudenko, J. Bartolomè, A. Arauzo, and Yu. V. Knyazev, *J. Magn. Magn. Mater.* **323**, 521 (2011).
29. N. B. Ivanova, N. V. Kazak, Yu. V. Knyazev, D. A. Velikanov, L. N. Bezmaternykh, S. G. Ovchinnikov, A. D. Vasiliev, M. S. Platunov, J. Bartolomè, and G. S. Patrin, *JETP* **113** (6), 1015 (2011).
30. E. A. Stern, *Phys. Rev. B: Solid State* **10**, 3027 (1974).
31. I. B. Borovskii, R. V. Vedrinskii, V. L. Kraizman, and V. P. Sachenko, *Sov. Phys.—Usp.* **29** (6), 539 (1986).
32. P. Eisenberg and B. M. Kincaid, *Chem. Phys. Lett.* **36**, 134 (1975).
33. G. M. Sheldrick, *Acta Crystallogr., Sect. A: Found. Crystallogr.* **64**, 112 (2008).
34. J. M. Tranguada and R. Ingalls, *Phys. Rev. B: Condens. Matter* **28**, 3520 (1983).
35. D. I. Kochubei, Yu. A. Babanov, K. I. Zamaraev, R. V. Vedrinskii, V. L. Kraizman, G. N. Kulipanov, L. N. Mazalov, A. N. Skrinskii, V. I. Fedorov, B. Yu. Khel'mer, and A. T. Shuvaev, *X-Ray Diffraction Method of Investigation of the Structure of Amorphous Solids (EXAFS Spectroscopy)* (Nauka, Novosibirsk, 1988) [in Russian].
36. M. Newville, *J. Synchrotron Radiat.* **8**, 322 (2001).
37. S. I. Zabinski, J. J. Rehr, A. Ankudinov, R. C. Albers, and M. J. Eller, *Phys. Rev. B: Condens. Matter* **52**, 2995 (1995).
38. F. de Groot, G. Vank'o, and P. Glatzel, *J. Phys.: Condens. Matter* **21**, 104207 (2009).
39. L. N. Bezmaternykh, S. N. Sofronova, N. V. Volkov, E. V. Eremin, O. A. Bayukov, I. I. Nazarenko, and D. A. Velikanov, *Phys. Status Solidi B* **249**, 1628 (2012).
40. P. W. Anderson, *Phys. Rev.* **115**, 1 (1959).
41. M. V. Eremin, *Sov. Phys. Solid State* **24** (2), 239 (1982).
42. O. A. Bayukov and A. F. Savitskii, *Phys. Solid State* **36** (7), 1049 (1994).
43. S. V. Vonsovskii, *Magnetism* (Nauka, Moscow, 1971; Wiley, New York, 1974).

Translated by K. Shakhlevich